Article ID：1007−7294(2026)06−0871−23

# Investigation on Porpoising Motion of Seaplane during Gliding on Waves

*LIU Wei−qin*[1,2], *PAN Zhen−feng*[1], *SONG Xue−min*[1,2], *HU Qi*[3,4], *WANG Ming−zhen*[3,4], *ZOU Qi−lu*[1]

(1. Key Laboratory of High Performance Ship Technology (Wuhan University of Technology), Wuhan 430063, China; 2. School of Naval Architecture, Ocean and Energy Power Engineering, Wuhan University of Technology, Wuhan 430063, China; 3. China Special Vehicle Research Institute, Jingmen 448000, China; 4. Key Laboratory of High-Speed Hydrodynamic Aviation Science and Technology, Jingmen 448000, China)

**Abstract:** Seaplanes are subjected to hydrodynamic forces, including slamming, splashing, and wave interference during aquatic operations. When planing or gliding on the water surface, seaplanes may experience slamming, where the aircraft impacts the water at high speed, resulting in significant vertical acceleration and impact forces. A numerical model of the aircraft was initially developed using Computational Fluid Dynamics (CFD). To account for the interaction between air and water, the Volume of Fluid (VOF) model was employed to solve the Reynolds-averaged Navier-Stokes equations. The Dynamic Fluid-Body Interaction (DFBI) method was applied to simulate the six-degree-of-freedom motion of the seaplane. Numerical simulations were performed at different gliding speeds. Next, the simulation results are compared with experimental data, validating the applicability of the numerical method for investigating the motion characteristics of the seaplane while gliding over waves. Finally, simulations under different wave conditions were carried out. The influence of wave parameters on the motion of the seaplane was investigated using the CFD method. The results indicate that the hydrodynamic load significantly affects the motion characteristics of the seaplane during gliding over waves.

**Key words: seaplane; Volume of Fluid (VOF); porpoising motion; gliding; hydrodynamic load**

**CLC number：** U661.1 **Document code：** A **doi:** 10.3969/j.issn.1007−7294.2026.06.003

## 0 Introduction

Seaplanes, capable of operating in both air and water, capitalize on the advantages offered by each environment. They are widely used in maritime rescue, reconnaissance, forest firefighting, and special operations. Due to their high environmental adaptability, seaplanes do not require large, specialized airports, thus conserving valuable land resources. Furthermore, seaplanes exhibit robust performance across diverse meteorological conditions and offer flexible deployment options for multi-role tasking. They are particularly useful for maritime patrol, anti-submarine operations, rescue missions, and forest firefighting. The advantages and versatility of seaplanes are considerable. Research into seaplanes holds strategic importance and economic value for the coastal countries, with promising application prospects.

Received date：2026−03−09

Foundation item：Supported by the National Natural Sicence Foundation of China (52101371; 52071243)

Biography：LIU Wei-qin (1985−), male, Ph.D., associate professor; PAN Zhen-feng (2001−), male, M.S.; SONG Xue-min (1986−), female, Ph.D., associate professor, corresponding author, E-mail: sxmxs@whut.edu.cn; HU Qi (1987−), male, M.S.; WANG Ming-zhen (1984−), male, M.S.; ZOU Qi-lu (1998−), female, M.S..

Seaplanes face several challenges when operating on water, such as slamming, splashing, and wave interference. During high-speed taxiing or water touchdown, slamming induces severe impulsive loads and substantial vertical accelerations. Slamming imposes significant loads on the aircraft, which can potentially damage the local structure. When moving in waves, the water jets sprayed from the bottom of the aircraft may splash onto the water surface, increasing the contact area between the fuselage and the water. This, in turn, raises the resistance during gliding, leading to higher engine power consumption and a reduction in gliding speed. Wave interference can cause the aircraft to bounce up and down on the water, reducing stability and maneuverability, while complicating the pilot operation. In severe cases, a phenomenon known as 'dolphin jumping' may occur, posing a serious threat to the aircraft's structural integrity and the safety of its passengers. These factors contribute to seaplane accidents, resulting in significant loss of life and property. Therefore, studying the gliding characteristics of seaplanes is essential.

Since the 1920s, numerous scholars and engineers have studied the load characteristics and structural properties of seaplanes. Early investigations primarily focused on the issue of water landing slamming, as this phenomenon is critical to the integrity and safety of the aircraft's overall structure. Over time, research has expanded to include concerns such as planing motion, splashing, and the dynamic simulation of the take-off process. In the mid-20th century, the study of seaplane load characteristics primarily relied on model tests and open-water model tests. While these model tests are intuitive, they are costly and constrained by the testing conditions. Systematic experimental studies were conducted by Klemin et al[1], Lina[2], Haines[3], Smith et al[4], Sottorf[5], and Ridland et al[6] to investigate the limiting conditions, influential factors, and prediction models for porpoising instability and slamming loads of seaplanes, providing guidance for their design.

With the advancements in computer technology, Computational Fluid Dynamics (CFD) simulations have become essential tools for studying seaplane-related issues. This method offers cost-effectiveness and high flexibility, effectively overcoming the limitations of traditional testing while enhancing applicability. The CFD approach overcomes the limitations of 2D+T (Sun and Faltinsen et al[7−9]) and other techniques in handling complex geometries and seaplanes with longitudinal step geometries. Qiu and Song[10] conducted a dynamic simulation of the seaplane take-off process using a decoupling algorithm, calculating aerodynamic and hydrodynamic forces separately. This dynamic analysis examined the interaction between the seaplane body and the water surface during take-off, in order to optimize the performance. Zheng et al[11−12] performed a numerical simulation of a seaplane model and compared the results with experimental findings, which showed good agreement; however, the discrepancy increased with velocity. Duan et al[13] investigated the porpoising phenomenon using a modified two-phase flow solver in OpenFOAM, simulating a large seaplane with four turbines during take-off. The complex effects, including hydrodynamic forces, aerodynamic forces, ground effect, and slipstream, were thoroughly considered. Zheng et al[14] studied the ditching performance of a blended-wing-body (BWB) aircraft using the CFD method, revealing the porpoising motion of the BWB aircraft, which was determined by a combination of hydrodynamic and aerodynamic loads. Song et al[15] studied the planing motion and hydrodynamic performance of a seaplane in calm water and waves, finding that the aerodynamic force in waves significantly influenced the seaplane motions. Deng et al[16] utilized CFD simulation to investigate the fuselage hydrodynamic behavior during taxiing, exploring the effects of various factors and proposing an effective scheme to improve numerical simulation.

In summary, extant literature on seaplane hydrodynamics has predominantly focused on interactions within calm water or low-amplitude wave environments. However, severe sea states significantly influence the hydrodynamic loads acting on the fuselage, thereby affecting seaplane motion—effects that are difficult to

capture in detail through experimental approaches. Therefore, a comprehensive understanding of porpoising behavior is essential for optimizing hull design, reducing slamming loads, and improving operational safety, particularly under rough sea conditions.

This study aims to achieve two main objectives. First, a coupled aerodynamic–hydrodynamic numerical method is investigated and validated for simulating seaplane gliding. Second, based on this coupled method, the motion characteristics and hydrodynamic loads of the seaplane during gliding in wave environments are analyzed. The findings aim to provide guidance for future seaplane design research. The paper is organized as follows: an introduction is presented, followed by a detailed description of the numerical methods used in this study, including the governing equations, turbulence models, the Volume of Fluid (VOF) method, and the DFBI model in Section 2. In Section 3, the numerical model is implemented and validated against experimental results. Section 4 presents simulations of seaplane gliding over various wave conditions, with a systematic analysis of the seaplane's motion and load characteristics. The influence of wave parameters on seaplane motion is examined using CFD methods. Finally, the main conclusions of this paper are presented in the final section.

## 1 Numerical methodology

The commercial CFD software STAR-CCM+ 16.06[17] is utilized in this study. The following key aspects are addressed in this section: the governing equations, the turbulence model for capturing the nonlinear phenomena in the simulation, the VOF model for representing the water-air interface, the Dynamic Fluid-Body Interaction (DFBI) model for simulating the coupling between fluid dynamics and seaplane rigid-body motion, and the relative motion between the seaplane and the water-air interface. The Finite Volume Method (FVM) is applied to solve the governing equations, providing information on the flow field and the seaplane. To account for the nonlinear phenomena associated with slamming, the turbulence model is employed in the simulation. The VOF model is utilized to solve the coupling between air and fluid. Fig.1 shows the flowchart of the numerical method applied in this paper.

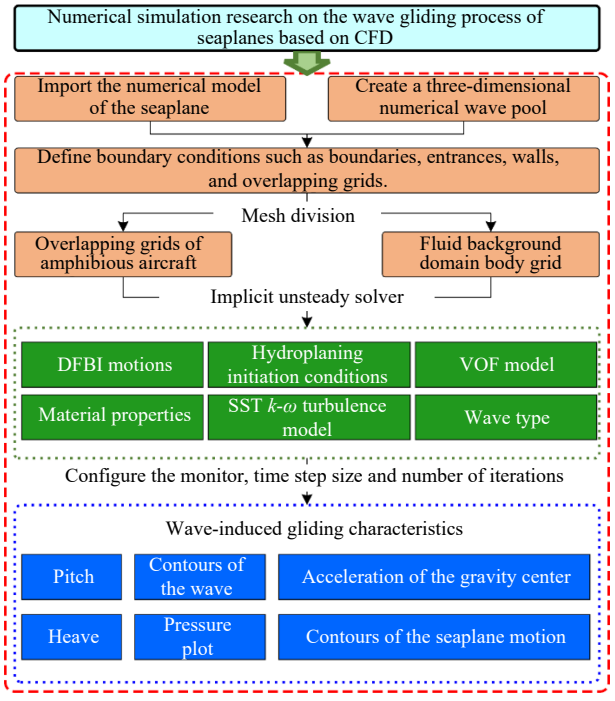



Fig.1 The flowchart of numerical method

### 1.1 Flow solver

In this study, the unsteady Reynolds-Averaged Navier-Stokes (RANS) equations are employed in conjunction with the SST $k$-$\omega$ turbulence model, which combines the advantages of both the $k$-$\omega$ and $k$-$\varepsilon$ models. The Semi-Implicit Method for Pressure-Linked Equations (SIMPLE) algorithm is utilized to resolve the pressure-velocity coupling. The pressure term is estimated using a weighted scheme that incorporates body forces, while the second-order upwind scheme is applied to the convection terms in the momentum and turbulence equations. The diffusion terms are approximated using a second-order central difference scheme,

and the unsteady terms are treated using a second-order implicit time integration method. More information on these numerical schemes is available in the STAR-CCM+ user guide.

**1.2 The governing equations**

The governing equations of Navier-Stokes equations are solved based on the conservation of mass and momentum for incompressible flow field with appropriate density and viscosity, as expressed in Eqs.(1) and (2). The SST $k$-$\omega$ turbulence model is employed to resolve the turbulence field. The mass conservation equation and momentum conservation equations are as follows

$$\frac{\partial u_i}{\partial x_i} = 0 \tag{1}$$

$$\frac{\partial u_i}{\partial t} + u_j \frac{\partial u_i}{\partial x_j} = -\frac{\partial P}{\partial x_i} + \frac{1}{\rho}\frac{\partial \tau_{ij}}{\partial x_j} + f_i \tag{2}$$

In the Cartesian coordinate system, the velocity vector is represented by $u_i$, where $P,\rho,\mu$ denote the pressure, density, and dynamic viscosity coefficient of the fluid, respectively. $\tau_{ij}$ is the shear stress tensor, defined as $\tau_{ij} = \mu(\partial u_i/\partial x_j + \partial u_j/\partial x_i).f_i$ represents the body force, such as gravity.

To simulate a realistic numerical environment for a towing tank, a numerical tank is constructed in the CFD framework, and the velocity inlet method is adopted to generate waves. The porous media method is used to absorb the reflected waves in order to prevent a reduction in wave accuracy due to reflection. Given the nonlinearities of wave loading, the VOF method is adopted to precisely capture the air-liquid interface. The phase volume fraction is used to determine the distribution and location of the air and water, as defined by the following equation

$$a_i = \frac{V_i}{V} \tag{3}$$

where $V_i$ is the volume of phase $i$ in one grid cell, and $V$ is the total volume of the gird cell. The sum of the volume fractions of all phases in one element must equal to 1. Based on the value of the volume fraction, the presence of different phases within the grid cells can be distinguished. Specifically, $a_i = 0$ indicates the absence of a phase in the corresponding grid cell, $0 < a_i < 1$ indicates the presence of multiple phases at the interface, and $a_i = 1$ indicates that the grid cell is fully occupied by a single phase.

**1.3 The VOF method**

The VOF method, proposed by Hirt and Nichols[18], is employed in the Finite Volume Method solver to capture free interfaces. The interface between liquid and gas is determined by calculating the volume fraction of two phases within each grid cell. The volume fraction $\alpha_{\text{water}}$ is introduced to represent the volume occupied by water. When the volume fraction $\alpha_{\text{water}}$ of water is between 0 and 1, a fluid interface exists in the cell. It is calculated using following equation

$$\alpha_{\text{water}} = \frac{V_{\text{water}}}{V} \tag{4}$$

where $V_{\text{water}}$ represents the volume of water in the grid cell, and $V$ represents the volume of the grid cell. The volume fraction of air in each cell can be computed as

$$\alpha_{\text{air}} = 1 - \alpha_{\text{water}} \tag{5}$$

For a grid cell with a free surface, the properties (such as density and dynamic viscosity coefficient) are weighted according to the different fluid phases.

$$\rho = \rho_{\text{air}}\alpha_{\text{air}} + \rho_{\text{water}}\alpha_{\text{water}} \tag{6}$$

$$\mu = \mu_{\text{air}}\alpha_{\text{air}} + \mu_{\text{water}}\alpha_{\text{water}} \tag{7}$$

where $\rho$ and $\mu$ represent the density and dynamic viscosity coefficients, respectively.

There are two main types of VOF schemes: algebraic and geometric VOF. The algebraic VOF model is used to capture the interface between water and air, with a water volume fraction of 0.5. The geometric VOF scheme, known as the High-Resolution Interface Capturing (HRIC) scheme, is one of the most widely used algorithms for interface tracking. The modified HRIC scheme facilitates the development of a stable interface while maintaining its boundedness.

**1.4 The DFBI method**

The Dynamic Fluid Body Interaction (DFBI) model is a numerical approach used to calculate the interaction between fluids and seaplanes. It is particularly well-suited for problems involving fluid-solid boundary interactions in dynamic systems. The DFBI model integrates fluid dynamics and structural mechanics simulations to predict the motion of the seaplane and the characteristics of fluid flow under dynamic loads.

The motion of the rigid body center is expressed as follows

$$m\frac{\mathrm{d}\vec{v}}{\mathrm{d}t}=\vec{F} \tag{8}$$

where $m$ represents the mass of the rigid body, $\vec{v}$ is the velocity of the mass center, and $\vec{F}$ represents the force acting on the rigid body.

The DFBI rotation equation is as follows

$$\vec{I}\dot{\vec{\omega}}+\vec{\omega}\times\vec{I}\vec{\omega}=\vec{n} \tag{9}$$

where $\bar{I}$ denotes the moment of inertia matrix, $\vec{\omega}$ represents the angular velocity, $\dot{\vec{\omega}}$ represents the angular acceleration vector, $\vec{n}$ is the moment. The moment of inertia is given by the following formula

$$\vec{I}=\begin{bmatrix} I_{xx} & I_{xy} & I_{xz} \\ I_{yx} & I_{yy} & I_{yz} \\ I_{zx} & I_{zy} & I_{zz} \end{bmatrix} \tag{10}$$

A numerical model of the seaplane is developed using the FVM method. To capture the air–fluid interaction, the VOF model is employed to solve the RANS. The DFBI method is implemented in all simulations to represent the six-degree-of-freedom motion of the seaplane. Subsequently, a series of numerical simulations is conducted at various gliding speeds and wave conditions.

## 2 Validation of the numerical method in seaplane gliding

This section presents the wave gliding motion test of a seaplane model. A CFD model is established based on the geometric parameters and boundary conditions of high-speed towing tank experiments. Initially, the computational domain—comprising background, overset, and refinement regions—was defined, followed by a mesh independence study to standardize the discretization scheme. Subsequently, a suitable turbulence model and boundary conditions are specified to ensure an accurate simulation of the seaplane model. Numerical simulations of the seaplane motion characteristics are then performed under nine operating conditions based on the model tests. The motion curves of the seaplane model are computed under coupled air and wave conditions. The numerical framework is validated by benchmarking the simulation results against experimental data.

**2.1 Physical model**

In this study, the aircraft model from the research on a 3.6 m seaplane model by Hu[19] is used as the subject of our numerical simulation. Fig.2 illustrates a three-dimensional diagram of the seaplane model. The overall design of the model is slender, featuring a V-shaped hull. The upper structure, comprising the wings

and tail fins, generates lift. To reduce water resistance and facilitate the introduction of air behind the steps, the underside of the seaplane is divided into two sections: the forebody and the afterbody. At low speeds, the forebody remains in contact with the water surface, providing buoyancy support. As speed increases beyond a certain threshold, the bow of the seaplane lifts out of the water. The main parameters of the seaplane model are detailed in Tab.1.

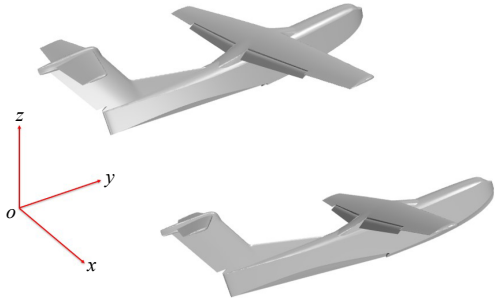



Fig.2 Diagram of the 3.6 m seaplane model

**Tab.1 Main parameters of the model**

| Main parameters | Value | Main parameters | Value |
|---|---|---|---|
| Length ($L$)/m | 3.6 | Initial trim angle/deg | 2.5 |
| Weight/kg | 60 | $I_{xx}$/(kg·m$^2$) | 18.314 |
| Wingspan/m | 1.8 | $I_{yy}$/(kg·m$^2$) | 20.153 |
| Waterline in floating/m | 0.125 | $I_{zz}$/(kg·m$^2$) | 35.970 |

The "water line in floating" refers to the draft of the model at the midship section under static floating condition, i.e., the vertical distance from the still waterline to the baseline at the midship.

**2.2 The CFD model and computational grids**

The geometric model of the aircraft is imported into STAR-CCM+. The entire flow field and overlapping region are then used to define the mesh scheme, as shown in Fig.3. The background domain, encompassing both the air and water phases, remains static to provide a stable medium for wave propagation. The overlapping domain is created by subtracting the model geometry, ensuring effective interaction between the aircraft and the background grid within the boundaries of the two regions. This configuration allows the model to move during the calculation process, enabling real-time interaction between the overlapping grid and the background grid, thereby ensuring effective information transmission between the two grids.

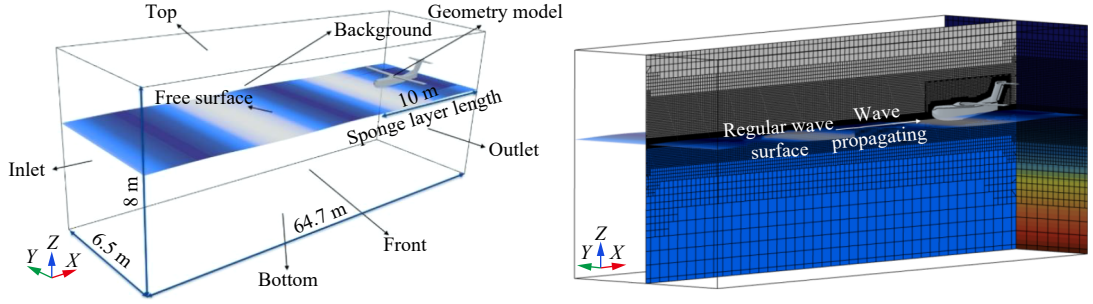



Fig.3 Computational domain and boundary conditions

The entire computational domain is carefully calibrated to match the dimensions of the high-speed towing tank, ensuring that the simulation conditions aligned with the actual test conditions. Accordingly, the background domain extents are defined from [−60.0 m, −3.25 m, −5.0 m] to [4.7 m, 0 m, 3.0 m]. The overlapping area is designated for simulating the motion of seaplanes and is required to fully encompass the entire seaplane geometry. Additionally, sufficient space is maintained between the seaplane geometry and the overlapping interface to allow for an adequate number of grid layers. This resolution is critical for resolving near-wall flow physics and ensuring an accurate boundary layer solution. Therefore, the size range for the design overlapping area is specified as [−0.2 m, −2.2 m, −0.5 m] to [4.5 m, 0 m, 1.2 m].

To calculate the motion of the seaplane during gliding in waves, a velocity-inlet boundary wave-maker is employed by prescribing wave phase velocities and phase functions at the inlet boundary of the

computational domain. First-order linear wave theory is utilized within the numerical tank for wave generation. The analytical solutions of the wave theory, expressed by Eqs.(11)~(15), are derived based on potential theory, which is used in all simulations.

$$\eta = \frac{H}{2}\cos(kx - \omega t) \tag{11}$$

$$\varphi = -\frac{Hg}{2\omega}\frac{\cosh k(h+z)}{\cosh kh}\sin(kx - \omega t) \tag{12}$$

$$u = -\frac{\partial \varphi}{\partial x} = \frac{H}{2}\frac{gk}{\omega}\frac{\cosh k(h+z)}{\cosh kh}\cos(kx - \omega t) \tag{13}$$

$$w = -\frac{\partial \varphi}{\partial z} = \frac{H}{2}\frac{gk}{\omega}\frac{\sinh k(h+z)}{\cosh kh}\sin(kx - \omega t) \tag{14}$$

$$\omega^2 = gk\tanh kh \tag{15}$$

In this context, $\eta$ represents the wave elevation, which varies at each $X$-axis position, $\phi$ is the velocity potential, $u$ denotes the water wave velocity in $x$-direction, while $w$ represents the fluid velocity in $z$-direction. $\omega$ refers to the angular velocity of the water wave, $H$ indicates the wave height, and $h$ is the water depth.

To prevent the reflection of waves at the boundary, a damping zone is introduced at the exit, extending over a distance of 1.5 to 2 times the wavelength. As shown in Fig.3, the wave elimination zone extends 12 m, positioned at the end of the wave tank. The damping coefficient is set to 1. Tab.2 presents the boundary types for both the overlapping and the background areas.

**Tab.2 Boundary conditions of the computational domains**

| Domain | Location | Boundary condition |
|---|---|---|
| Background domain | Inlet | Velocity inlet |
| | Outlet | Pressure outlet |
| | Front | Wall |
| | Background | Wall |
| | Top | Pressure outlet |
| | Bottom | Wall |
| Overlapping domain | Geometry model | Wall |
| | Interface between background and overlapping domain | Overset mesh |

### 2.3 Grid independence analysis

In CFD simulations, mesh size plays a critical role in both the efficiency and accuracy of numerical analysis. For aircraft gliding simulations, techniques such as surface reconstruction, automatic surface repair, volume mesh generation, and prismatic layer mesh generation are employed to create both surface and volume meshes for the background and overlapping domains. To accurately capture phenomena such as boundary layer effects near the surface of the seaplane and variations in the free liquid surface flow, it is essential to define surface and volume controls that allow for finer mesh divisions. Additionally, volume control refinement is applied in the background region to ensure that the mesh size at the overlapping interface closely matches that of the background domain. This approach minimizes data interpolation errors between the overlapping region and the background domain, thereby improving the accuracy of the computational results.

A grid independence analysis is conducted with the simulation condition set to a wave height of 0.07 m and a wavelength of 1 m. The various base grid sizes, and the specific details of the meshes utilized are presented in Tab.3. The schematic of the mesh for numerical wave generation is shown in Fig.4.

**Tab.3 Details of the meshed used in the simulations**

| Grid scheme | Number of all grids | Number of background grids | Number of overset grids | Mesh size/mm |
|---|---|---|---|---|
| Mesh A | 7 773 644 | 4 420 984 | 3 352 660 | 10.94 |
| Mesh B | 10 416 646 | 5 859 188 | 4 557 458 | 3.69 |
| Mesh C | 13 115 111 | 7 675 760 | 5 439 351 | 1.74 |

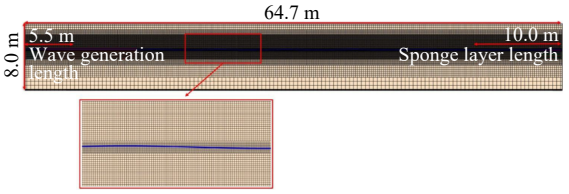



Fig.4 Schematic of the mesh for wave generation

The total number of grids in the coarse Mesh A is approximately 777 364, while the medium Mesh B contains about 10 416 646 grids, and the fine Mesh C consists of approximately 13 115 111 grids. These three grid schemes are employed in the seaplane gliding simulations. The wave height time-domain curves for the three grid schemes are shown in Fig.5. It is evident that the wave height changes periodically, and the trends are consistent across all three grid sets, indicating their suitability for the numerical simulation of seaplanes. The wave height for Mesh A is 64.72 mm, with a deviation from the theoretical value of 7.54%. The wave height for Mesh B is 65.98 mm, with a deviation of 5.74%. The wave height for Mesh C is 66.78 mm, with a deviation of 4.60%. Considering both the accuracy and efficiency of the results, the medium grid scheme Mesh B is selected for the numerical simulation of seaplane gliding in calm water and waves. The data were averaged and compared with the theoretical value. The wave amplitude values are presented in Tab.4. To estimate the uncertainty in the numerical solution, the results obtained using Mesh A, B, and C are denoted as $s_1$, $s_2$, and $s_3$, respectively. $\varepsilon_{12}$ and $\varepsilon_{23}$ denote the differences between the results obtained using Mesh B and Mesh A, and between Mesh C and Mesh B, respectively

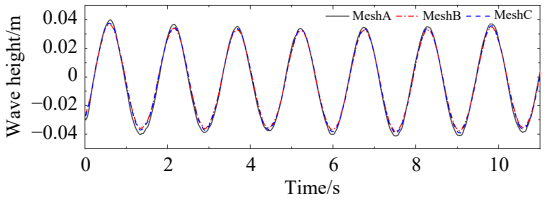



Fig.5 The time history of the wave elevation for all grid schemes

**Tab.4 Verification of numerical results**

| Numerical results | $s_1$ | $s_2$ | $s_3$ | $\varepsilon_{12}$ | $\varepsilon_{23}$ | $R_k$ |
|---|---|---|---|---|---|---|
| Mean wave height/mm | 64.72 | 65.98 | 66.78 | 1.26 | 0.8 | 0.63 |

$$\varepsilon_{12} = s_2 - s_1 \tag{16}$$

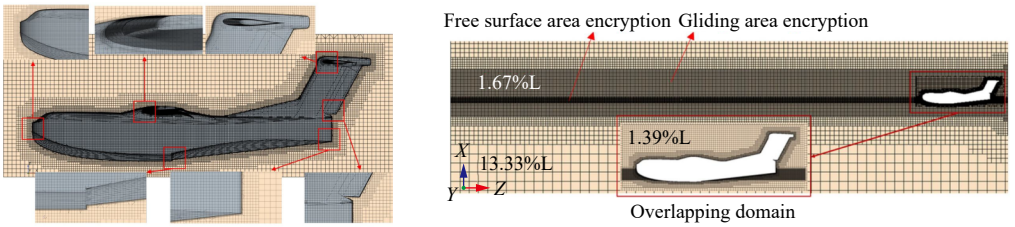
$$\varepsilon_{23} = s_3 - s_2 \tag{17}$$

The convergence rate $R_{ki}$ is calculated as

$$R_{ki} = \frac{\varepsilon_{i,i+1}}{\varepsilon_{i-1,i}} \tag{18}$$

The convergence rate can be classified into three types of numerical solutions: 1) $0<R_k<1$, indicating monotonic convergence, 2) $R_{ki}<0$, indicating oscillatory convergence, and 3) $R_{ki}>1$, indicating divergence. As shown in Tab.4, the results demonstrate monotonic convergence with respect to the mesh size. This suggests that, considering the grid dimensions referenced in the relevant literature and the computational cost-effectiveness, selecting Mesh B is a viable choice for future studies.

In the final seaplane grid scheme, the basic mesh size on the body surface is 0.01 m, while the base mesh size in the overlapping domain is 0.05 m. The base mesh size in the background region is 0.12 m. The free surface in the $x$- and $z$-directions within the computational domain is locally refined, resulting in a mesh size of 0.025 m in the $x$ direction and 0.007 m in the $z$ direction within the overlapping domain (indicating that each wave height is represented by 10 grid points). In the background domain, the mesh size of the liquid surface is 0.03 m in both the $x$ and $z$ directions. The grid division near the profile is shown in Fig.6(a).




（a）Mesh refinement on the seaplane surface　　（b）Mesh refinement for the wave

Fig.6 The schematic of grid scheme

As reported in previous studies, turbulent modelling and mesh size are crucial factors in simulating seaplane motion in waves (Qiu et al[10], Jafar et al[20] and Zheng et al[11]). Consequently, localized refinement in the vicinity of the hull is imperative to resolve high-speed slamming and associated nonlinear phenomena. Based on grid independence analysis, a mesh size of 1.39% of the length ($L$) is adopted to refine the surface of the seaplane. Additionally, it is important to implement uniform grids around the free surface. Due to the differences in the densities and viscosities of water and air, the coupled aerodynamic and hydrodynamic simulations require the hydrodynamic non-dimensional distance $y+$ value to be at least 10 times greater than that of the aerodynamic $y+$ value. In the model-scale coupled aerodynamic and hydrodynamic calculations, the $y+$ values in the water domain ranged from 30 to 60, while in the air domain, they ranged from 0 to 1. The first layer grid height is set globally at 0.45 mm for practical purposes. Finally, to ensure accurate simulations, a total of approximately 10.6 million meshes are used, as shown in Fig. 6 (b).

**2.4 Validation against the experiment results**

In this section, the simulation of the seaplane gliding over waves is investigated based on the FVM solver. The unsteady RANS equations are solved in conjunction with the SST $k$-$\omega$ turbulence model. Pressure-velocity coupling is handled using the SIMPLE algorithm, and second-order upwind schemes are applied to discretize the convection terms in both the momentum and turbulence equations. An implicit second-order unsteady time discretization method is employed, with a time step of 0.005 s, as recommended by ITTC[21]. The temporal evolutions of heave, pitch, and center-of-gravity acceleration were extracted and validated against experimental data. A series of numerical simulations are performed using the validated method. The seaplane's initial condition is set to be the same as that in the reference by Hu et al[19], the simulation conditions are set as shown in Tab.5.

**Tab.5 Simulation conditions for validation**

| Case | Speed/(m·s$^{-1}$) | Relative wave length | Wave height/m |
|---|---|---|---|
| 1 | 3 | 2 | 0.07 |
| 2 | 9 | 2 | 0.07 |
| 3 | 3 | 2 | 0.3 |

Cases 1, 2, and 3 represent extreme conditions characterized by the longest wavelength, highest speed, and greatest wave height, respectively. Under these conditions, the interaction between the seaplane and the water surface becomes more pronounced, resulting in significant wave impacts and splashes that present a considerable challenge to the seaplane's hydrodynamic performance and structural integrity. Assessing the seaplane's performance under such extreme conditions is crucial. Since the seaplane must perform a gliding motion within the background domain during numerical simulations, a larger background domain is required, which in turn demands substantial computational resources. Consequently, all test cases in this section are limited to a time frame of 5 seconds.

In Cases 1 and 2, the heave motion of the seaplane is extracted and compared with experimental results. As shown in Fig.7, the solid black line represents the simulation values for the heave motion of the seaplane, while the dotted red line represents the experimental values. For Cases 1 and 2, when the seaplane glides through the waves, the simulation results align with the trends observed in the experimental results. In Case 1,

the amplitude of the heave motion obtained from the numerical simulation is 74.3 mm, whereas the amplitude from the experimental data is 70 mm, resulting in an error of 6.1%. In Case 2, the amplitude of the heave motion from the numerical simulation is 101.3 mm, compared to 92.778 mm from the experimental data, yielding an error of 8.68%. This discrepancy falls within the acceptable range for practical engineering applications. It is also indicated that the heave curves exhibit a sinusoidal pattern which is consistent with the periodicity of the waves. The period of the simulated motion closely matches that of the experimental results. Although there is a minor deviation in amplitude, which can be attributed to model simplifications and approximations in wave generation and propagation, this deviation remains within the acceptable range of engineering error. These findings validate the fidelity of the numerical model, confirming its suitability for investigating seaplane hydrodynamics. Due to the absence of experimental data, Case 3 focuses on investigating the heave motion of a seaplane gliding under conditions of relatively high wave amplitude, which exhibits similar behavior to pitch and vertical acceleration.

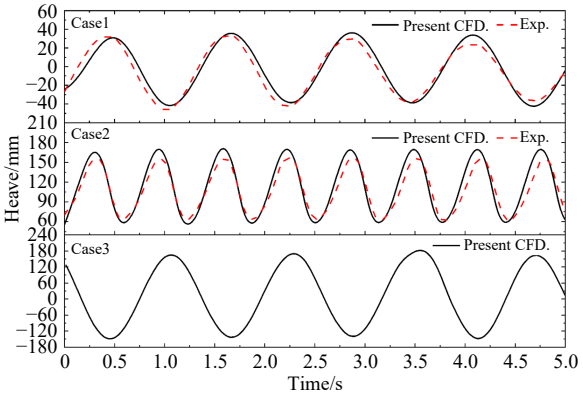



Fig.7 Time history of the heave motion for Cases 1, 2, and 3

Fig.8 shows the time history of the pitch motion for Cases 1, 2, and 3. The solid black line in the figure indicates the simulation values for pitch motion, while the dotted red line represents the experimental values. It can be observed that when the seaplane glides over the waves, the pitch curves exhibit sinusoidal patterns, reflecting the periodic nature of the seaplane motion, which corresponds to the periodicity of the waves. In Case 1, the simulation result for the pitch motion is 2.616°, whereas the experimental result is 2.651°, yielding an error of 1.32%. Similarly, in Case 2, the simulation result for the pitch motion is 12.785°, while the experimental result is 12.704°, resulting in an error of 0.63%. In Case 2, the discrepancy between the simulation and experimental results can be attributed to the high speed of the seaplane.

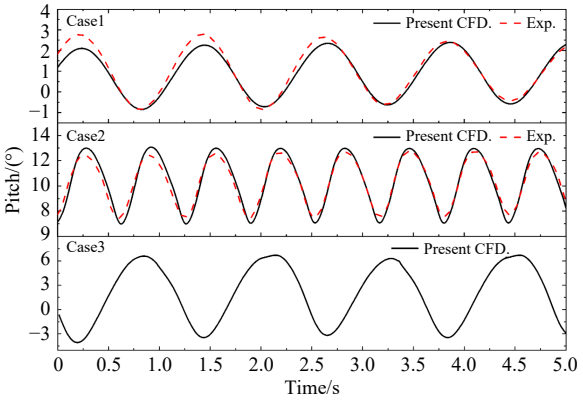



Fig.8 Time history of the pitch motion for Cases 1, 2, and 3

Compared to the time-history curve of motion response in Cases 1 and 2, it is evident that an increase in wave height leads to a corresponding increase in the amplitude of the motion response. This indicates that higher wave heights subject the seaplane to greater dynamic loads, resulting in increased heave and pitch motions. However, this increase does not fundamentally alter the speed of the seaplane, nor does it affect the ratio of the forces generated by the combined effects of lift and hydrodynamic forces produced by the wings. As a result, the motion response under these conditions remains periodic and consistent with the periodic characteristics of the waves.

Fig.9 shows the time history of the vertical acceleration in Cases 1, 2, and 3. The solid black line in the figure indicates the simulation values; the results are obtained directly from the simulations and divided by the acceleration due to gravity. For Cases 1 and 3, the vertical acceleration curves at the center of gravity exhibit a sinusoidal pattern, reflecting the periodic nature of the aircraft motion and corresponding to the

periodicity of the waves. In Case 2, however, it is demonstrated that at a speed of 9 m/s, the vertical acceleration at the center of gravity no longer follows a linear pattern; instead, two distinct peaks emerge. When compared to the time history obtained from numerical simulations, the peaks in the time curve derived from the model test are more pronounced. This suggests significant discrepancies between the numerical simulation results and the actual test data during high-speed maneuvers, indicating certain limitations of the digital simulation model. Nevertheless, despite these differences, the consistent trends observed in both datasets suggest that the simulation model is capable of effectively predicting the motion characteristics of the aircraft under wave conditions. In Case 1, the simulation result for vertical acceleration is 0.201 *g*, while the experimental result is 0.188 *g*, yielding an error of 6.9%. In contrast, Case 2 exhibits a significant nonlinear variation in acceleration. Due to the impact on the water surface, the acceleration variation follows a double-peak pattern. The peak acceleration recorded in the test for the seaplane at this speed is 0.896 *g*, while the peak value from the numerical simulation is 0.935 *g*, resulting in an error of 3.49%.

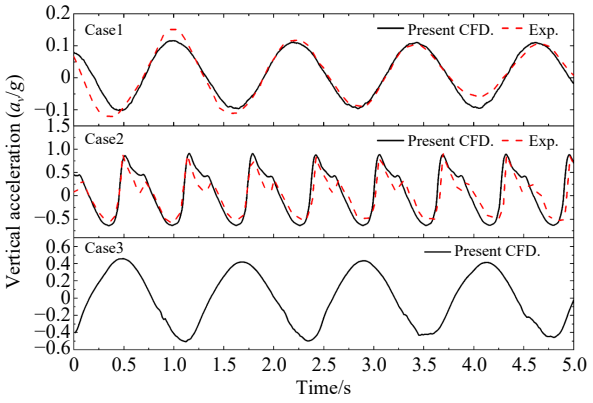
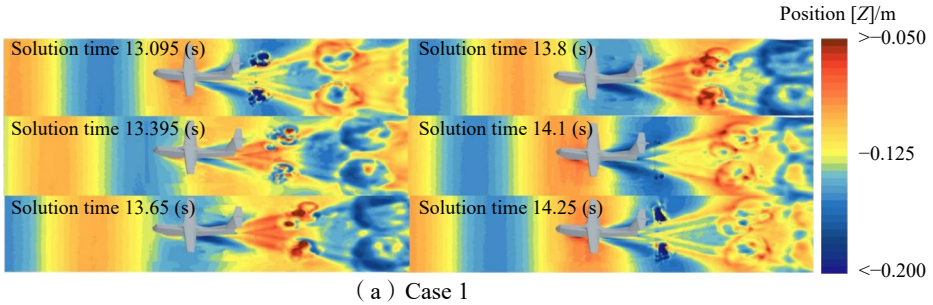



Fig.9 Time history of vertical acceleration for Cases 1, 2, and 3

The vertical acceleration of the center of gravity in Case 2 indicates that, as speed increases, the acceleration of the seaplane's center of gravity no longer follows a linear pattern. This nonlinearity becomes more pronounced at higher speeds. This is due to the fact that increased speed alters the interaction between the aircraft and the water, which affects the distribution of drag and lift forces. The wings generate significant lift, which influences the vertical motion of the aircraft, leading to variations in the vertical acceleration of the center of gravity.

Fig.10 illustrates the simulated contours of the seaplane gliding in one cycle of a wave in Cases 1, 2, and 3. In Case 1, these contours reveal the phenomenon of bow lifting during the seaplane movement, resulting in the formation of a standard Kelvin wave behind its body. Bow lifting is a natural response of seaplanes under specific sea conditions and speeds, helpful to reduce water resistance and providing additional lift. The presence of Kelvin waves indicates that the hydrodynamic characteristics of the seaplanes under these conditions exhibit linear behavior, specifically that no splashing or other nonlinear phenomena occur when the speed is low and the movement is gentle. In Case 2, the wave pattern behind the body is disturbed, suggesting that the hydrodynamic characteristics of the seaplane at high speeds differ substantially from those at lower speeds, leading to nonlinear phenomena. In Case 3, no splashing or other nonlinear hydrodynamic phenomena are observed, indicating that the hydrodynamic characteristics remain linear. In other words, at low speeds and with minimal movement, the seaplane does not produce splashes or other nonlinear effects.




（a）Case 1

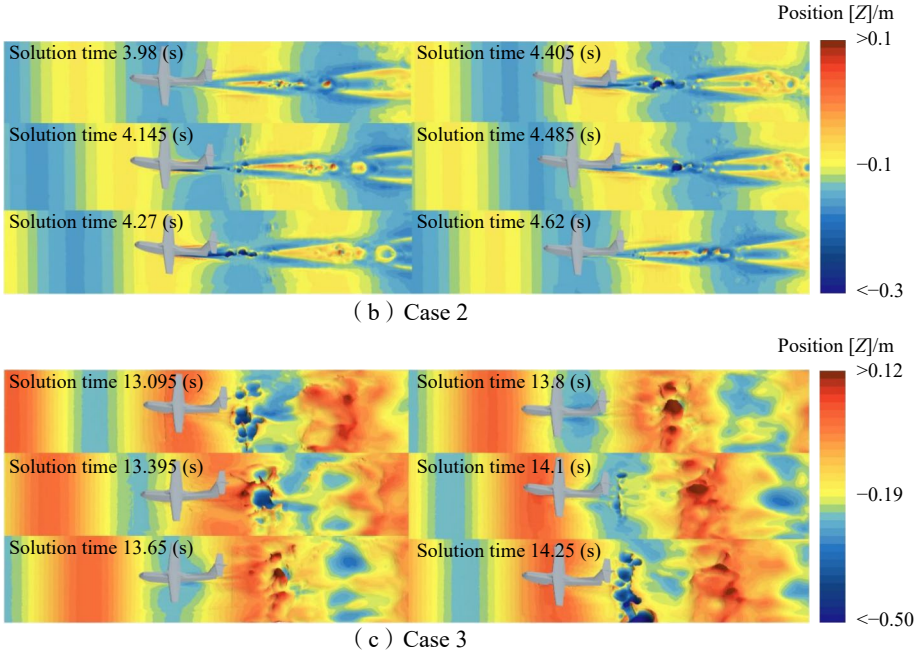



Fig.10 The contours plots of the seaplane during one wave cycle

Fig.11 presents the motion of the seaplane during a complete wave cycle. The side view of the seaplane gliding is shown in this figure. Four instantaneous positions of the aircraft on the wave surface during one cycle are depicted in Fig.11, offering a clear understanding of the seaplane's gliding behavior under these conditions. It is observed that the wetted area of the fuselage is the largest at the downward wave position during the cycle, resulting in the greatest horizontal pressure and shear loads. The numerical simulation identifies distinct phenomena, such as porpoising motion, occurring during the seaplane's glide over the

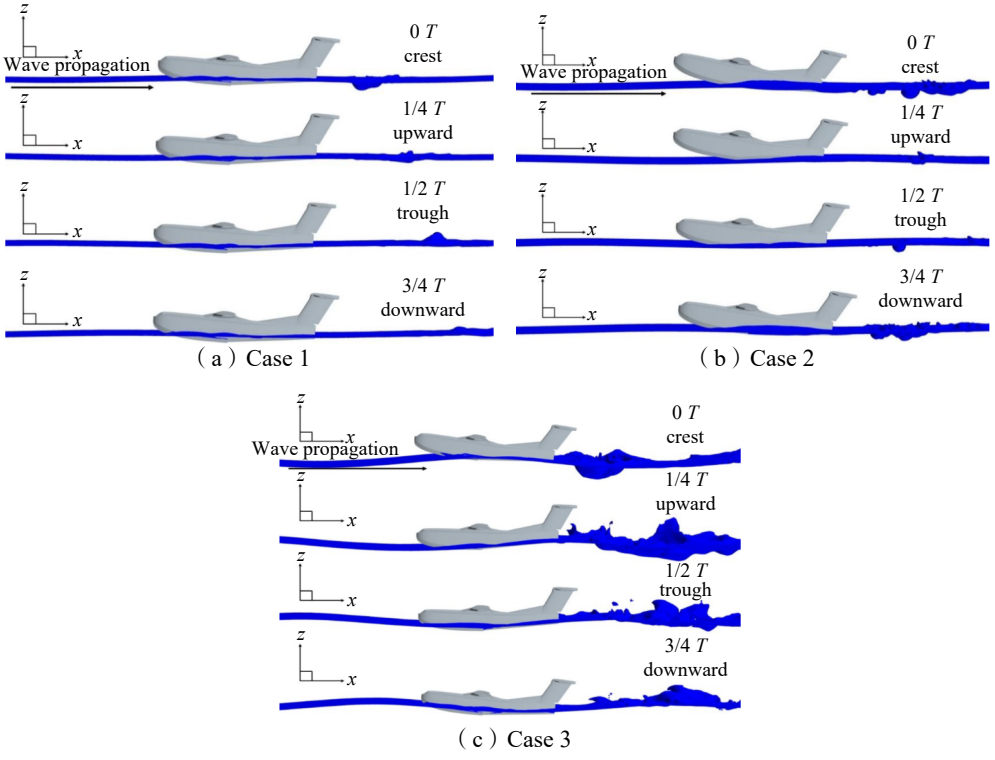



Fig.11 Four instantaneous aircraft positions on wave surface in one period

waves. This behavior directly arises from the interaction between the seaplane and the waves. This result suggests that the seaplane exerts a significant influence on the surrounding water flow while gliding in Case 3.

The results of Cases 1 and 2 are compared with experimental data and show good agreement, confirming that the coupled aerodynamic-hydrodynamic solver is appropriate for simulating seaplane gliding in wave conditions. Case 3, which involves high wave heights, explores seaplane motion under such conditions; however, it has not been validated due to the absence of corresponding experimental data. As indicated by the results, the current model does not incorporate multiphase phenomena such as cavitation, surface fragmentation, or spray formation, which may become significant at higher velocities.

## 3 Simulation of seaplane gliding in waves

The motion amplitude of the seaplane model reflects the intensity of rigid-body motion. Corresponding motion amplitudes from both model tests and numerical simulations under various operating conditions are extracted for comparative analysis. Given that the amplitude fluctuates across different conditions, the average amplitude over a 5-second time interval is used to represent the motion amplitude. This approach minimizes the impact of momentary data fluctuations and ensures a more stable and reliable analysis of the results. Data from nine operating conditions of the seaplane are processed, and the heave, pitch, and vertical acceleration at the center of gravity are statistically analyzed.

### 3.1 Simulation conditions

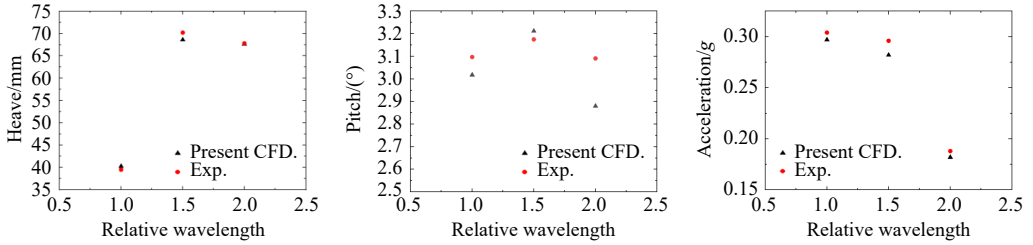
A case scheme for the numerical study has been developed based on the conditions of the seaplane model experiments. Nine conditions are examined through numerical simulations, as detailed in Tab.6. This scheme investigates the effects of wavelength, towing speed, and wave height on the motion characteristics of the seaplane. The relative wavelength is defined as the ratio of the wavelength to the total length of the seaplane. The impact of wavelength is analyzed in Cases S1 to S3, with relative wavelengths of 1, 1.5, and 2, respectively. The effect of towing speed is evaluated in Cases S3 to S6, with towing speeds of 3 m/s, 6 m/s, 8.5 m/s, and 9 m/s. The influence of wave height is examined in Cases S3 and S7 to S9, with wave heights of 0.07 m, 0.1 m, 0.2 m, and 0.3 m, respectively.

**Tab.6 Verification of simulation conditions**

| Case | Type | Towing speed/(m·s$^{-1}$) | Relative wave length | Wave height/m |
|---|---|---|---|---|
| S1 | Variable wave length | 3 | 1 | 0.07 |
| S2 | | 3 | 1.5 | 0.07 |
| S3 | | 3 | 2 | 0.07 |
| S3 | Variable speed | 3 | 2 | 0.07 |
| S4 | | 6 | 2 | 0.07 |
| S5 | | 8.5 | 2 | 0.07 |
| S6 | | 9 | 2 | 0.07 |
| S3 | Variable wave height | 3 | 2 | 0.07 |
| S7 | | 3 | 2 | 0.1 |
| S8 | | 3 | 2 | 0.2 |
| S9 | | 3 | 2 | 0.3 |

### 3.2 Effect of wave length on seaplane response

The influence of different wavelengths on the motion response of a seaplane during wave taxiing is investigated at a fixed speed and wave height. The amplitudes of heave, pitch, and vertical acceleration at the center of gravity of the seaplane are measured at a speed of 3 m/s and a wave height of 0.07 m across various wavelengths. The amplitude data for Cases S1 to S3 are extracted and plotted, as shown in Fig.12. It is observed that, under the fixed speed (3 m/s) and wave height (0.07 m), the experimental and simulation results exhibit consistent trends.




（a）Heave （b）Pitch （c）Vertical acceleration at the center of gravity

Fig.12 The motion of the seaplane under variable relative wavelength

The heave and pitch motions of the seaplane exhibit a non-monotonic trend with changes in wavelength. Initially, these motions increase with the wavelength, reaching a maximum at approximately 1.5 times the seaplane length, before decreasing. For shorter wavelengths, the higher wave frequency causes the seaplane to encounter more peaks and troughs within each wave cycle, thereby increasing the amplitudes of both heave and pitch motions. The heave and pitch amplitudes are maximized when the wavelength is approximately 1.5 times the seaplane's length. This phenomenon likely occurs because, at this specific wavelength, the wave period closely aligns with the natural vibration period of the seaplane, resulting in a resonance effect that amplifies the motion response. When the wavelength exceeds 1.5 times the length of the aircraft, the wave frequency decreases, and the seaplane encounters fewer peaks and troughs within each wave cycle. Consequently, the wave period lengthens, no longer matching the natural vibration period of the seaplane, reducing the resonance effect and potentially decreasing the amplitudes of the heave and pitch motions. Tab.7 presents the simulation and experimental results normalized by the wavelength. The results indicate that both heave and pitch reach their maximum values when the wavelength is 1.5 $L$.

**Tab.7 The simulation and experimental results of the seaplane motion responce under different relative wavelengths**

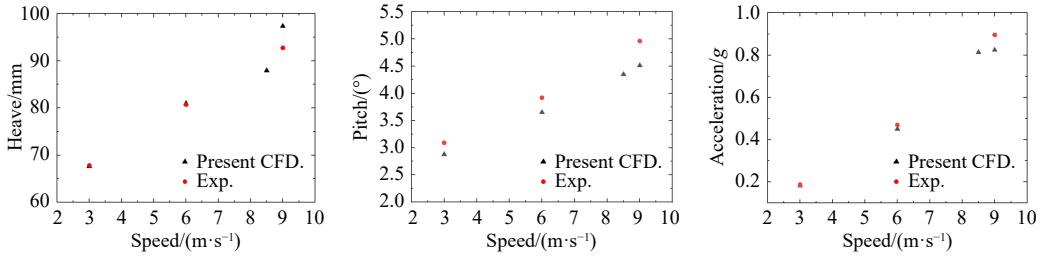
| Items | Simulation results | | | Experimental results | | |
|---|---|---|---|---|---|---|
| Relative wavelength | Heave/(m/m) | Pitch/(deg/m) | Acceleration/(m·s$^{-2}$) | Heave/(m/m) | Pitch/(deg/m) | Acceleration/(m·s$^{-2}$) |
| $L$ | 1.15 | 86.23 | 8.49 | 1.13 | 88.49 | 8.69 |
| 1.5 $L$ | 1.96 | 91.77 | 8.06 | 2.01 | 90.71 | 8.46 |
| 2 $L$ | 1.93 | 82.29 | 5.20 | 1.94 | 88.31 | 5.37 |

The vertical acceleration of the seaplane center of gravity decreases as the wavelength increases. As a wave propagates across the water, its energy is distributed in the direction of propagation. Longer wavelengths result in energy being spread over a larger horizontal area, leading to relatively small vertical amplitudes for individual crests and troughs. The vertical acceleration at the center of gravity is influenced by the vertical forces generated by the waves. As the wavelength increases, the wave energy is distributed over a broader horizontal range, rather than being concentrated directly beneath the seaplane. This distribution reduces the direct impact on the center of gravity of the seaplane, thereby decreasing the vertical acceleration as the wavelength increases.

### 3.3 Influence of gliding speed on porpoising behavior

The influence of varying speeds on the motion response of a seaplane is investigated while maintaining a constant wave height and wavelength. The amplitudes of heave, pitch, and vertical acceleration at the center of gravity of the seaplane are recorded at different speeds, with a wave height of 0.07 m and a relative wavelength of 2. Amplitude data from Cases 3 to 6 are extracted, as shown in Fig.13. The amplitudes of

heave, pitch, and vertical acceleration increase with gliding speed. The discrepancy between experimental and simulation results also increases with gliding speed, as higher speeds result in greater impact forces and more pronounced porpoising motion. Additionally, capturing the slamming phenomenon in numerical simulations remains challenging.

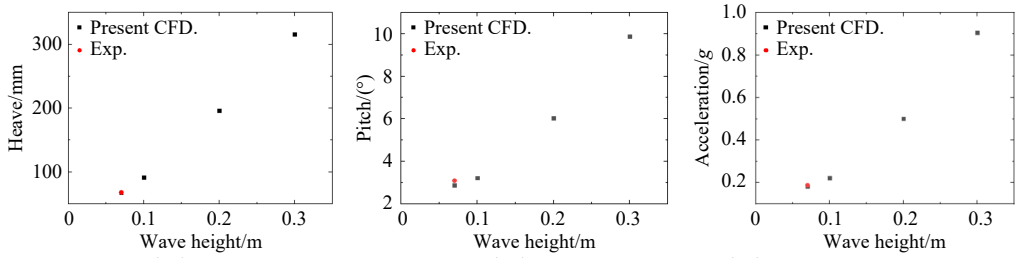



（a）Heave　（b）Pitch　（c）Vertical acceleration at the center of gravity

Fig.13 The motion of the seaplane under variable relative wavelength

### 3.4 Role of wave height in vertical acceleration

The effects of varying wave heights on the motion response of a seaplane are investigated at a fixed speed and wavelength. The amplitudes of heave, pitch, and vertical acceleration at the seaplane's center of gravity are measured for different wave heights, specifically at a speed of 3 m/s and a relative wavelength of 2. The amplitudes for Cases S3, S7, S8, and S9 are extracted, as shown in Fig.14.




（a）Heave　（b）Pitch　（c）Vertical acceleration at the center of gravity

Fig.14 The motion of the seaplane under variable wave height

It can be observed that, under conditions of a fixed speed (3 m/s) and a relative wavelength of 2, the heave, pitch, and vertical acceleration of the center of gravity of the seaplane increase as wave height increases. This trend is consistent with the simulation results. Wave height directly reflects wave energy, with an increase in wave height indicating that the wave carries more energy. When the wave interacts with the seaplane, a larger amount of energy is transferred to the aircraft. As a result, higher waves exert a more significant impact on the seaplane, leading to an increase in the amplitude of the motion response.

### 3.5 Impact load

To monitor the impact load on a seaplane hull during wave-induced gliding and to analyze its response characteristics, the forecastle of the fuselage is defined as the origin, and the coordinates of each measurement point are non-dimensionalized. Positions along the $X$-axis are scaled by $L/30$, and those along the $Y$-axis by $B/4$ ($B$ is the width of the seaplane). A total of 20 measurement points are distributed over 8 transverse sections (3, 6, 9, 15, 17, 21, 26, and 29) along the longitudinal direction above the bow, and across 4 longitudinal sections (0, 1, 2, and 4) in the transverse direction above the mid-longitudinal plane, as shown in Fig.15. Among them, measurement points 1 to 12 are located forward of the bottom step break, while points 13 to 20 are positioned aft of the break. Measurement points 5 and 7 are symmetrically located on the

starboard and port sides of the fuselage, respectively, to verify structural symmetry, as listed in Tab.8.

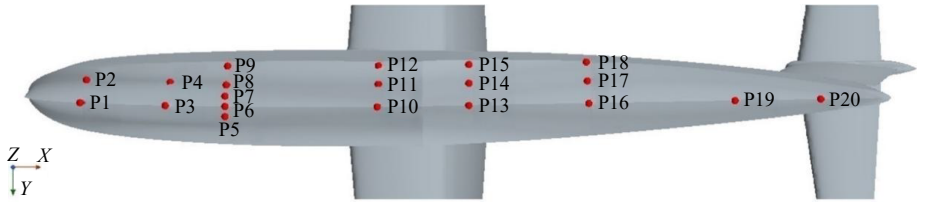



Fig.15 Layout diagram of pressure measurement points at the bottom of the seaplane

**Tab.8 The positions of the pressure measurement points**

| *X*/(*L*/30)<br>*Y*/(*B*/4) | 3 | 6 | 9 | 15 | 17 | 21 | 26 | 29 |
|---|---|---|---|---|---|---|---|---|
| Longitudinal section 1 | 1 | 3 | 5 | 10 | 13 | 16 | 19 | 20 |
| Longitudinal section 2 | | | 6、7 | | | | | |
| Longitudinal section 3 | 2 | 4 | 8 | 11 | 14 | 17 | | |
| Longitudinal section 4 | | | 9 | 12 | 15 | 18 | | |

To ensure stable numerical solutions, this study commences data collection after the simulation achieved steady-state conditions over several wave cycles. The slamming pressure data recorded at the fuselage bottom of the numerical model are then normalized using the following dimensionless coefficient for peak slamming pressure

$$\Pi_P = P/\rho v^2 \tag{19}$$

where $P$ is the measured point pressure value, $\rho$ is the fluid density, $v$ is the operational speed.

Due to the extensive pressure data collected from the seaplane, several measurement points under typical conditions have been selected to investigate the load characteristics of the seaplane in various sea states. This study also examines the distribution patterns of loads along the transverse and longitudinal axes of the seaplane. When the seaplane glides through waves, different sections of the aircraft experience varying degrees of load and stress due to the dynamic effects of the waves. The bow and stern, being the initial contact points with the waves, are particularly susceptible to slamming, while the midsection serves as the primary area for bearing wave loads. Consequently, a total of five bottom pressure measurement points (P3, P10, P11, P12, and P19) have been selected from the bow, midsection, and stern regions of the seaplane for analysis.

Based on the numerical simulation data from Case 1, partial pressure measurement points are selected for a comparative analysis of hull slamming pressure. In Fig.16, the measurement points in the same longitudinal section are grouped together. For example, the red line shows the pressure at measurement points in longitudinal section 1, the black line indicates the pressure at measurement points in longitudinal section 2, the orange line shows the pressure at measurement points in longitudinal section 3, and the blue line shows the pressure of measurement points in longitudinal section 4. In Case 1, the speed is 3 m/s, the relative wavelength is 2, and the wave height is 0.07 m. In this scenario, the recorded peak load at measurement points gradually decreases with increasing distance from the centerline plane on the same transverse section. This observation indicates that the fuselage is primarily influenced by wave loads, suggesting that the structural design near the

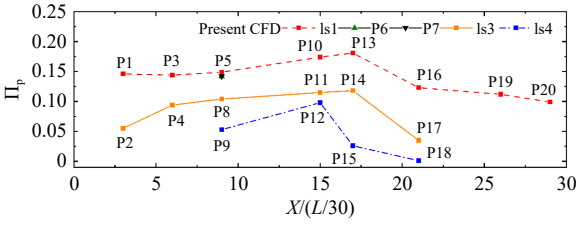
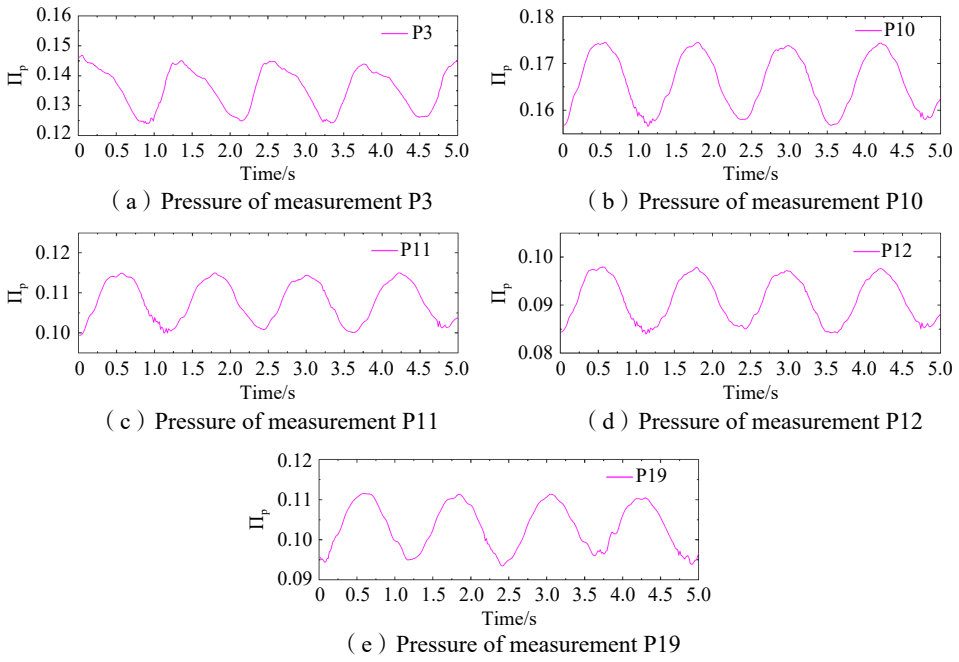



Fig.16 Longitudinal distribution of impact load in Case 1

centerline plane of the fuselage bottom is critical, as this region experiences the maximum pressure. Among all the measurement points, Point 13 recorded the highest pressure due to the depth of water entry at this location.

Fig.17 shows the time history of pressure at the measurement points (P3, P10, P11, P12, and P19). The points (P10, P11, P12, and P19) located in the midsection and stern of the body exhibit a sinusoidal pattern. This suggests that the pressure fluctuations at these locations are periodic, with no significant nonlinear phenomena detected. The presence of sine curves aligns with the periodic nature of wave motion, indicating that the pressure variations in these regions are predominantly influenced by the periodic effects of waves. In contrast, the time-domain curve at the bow measurement point 3 reveals a more pronounced nonlinear slamming phenomenon in the real model. This observation suggests that the hydrodynamic interactions at the bow are more complex, potentially involving wave breaking, splashing, or other nonlinear effects. The emergence of such nonlinear phenomena requires careful consideration during the design process, as they may introduce additional loads and stresses that could compromise the structural integrity and performance of the seaplane.




（a）Pressure of measurement P3　（b）Pressure of measurement P10

（c）Pressure of measurement P11　（d）Pressure of measurement P12

（e）Pressure of measurement P19

Fig.17 Time histories of pressure at selected measurement points

Fig.18 illustrates the pressure contours of the seaplane's bottom during one wave cycle for Case 1. Throughout the taxiing process, the pressure on the fuselage surface is symmetrically distributed along the mid-longitudinal section of the aircraft. The step breakdown structure of the seaplane induces local acceleration of the water flow at the step, leading to alterations in the pressure distribution. Consequently, this generates sudden fluctuations at the pressure monitoring points in this region. It can be observed that the pressure experienced during the planing process primarily occurs in the midsection of the aircraft. Additionally, the peak in the time-domain at the middle position is the most significant.

The analysis of hull slamming pressure data for the pressure measurement points in Case 2 reveals that, under these conditions, the peak load recorded by the measurement points gradually decreases as the distance from the centerline plane increases. This trend suggests that the seaplane is primarily influenced by wave loads, making the structural design near the centerline plane of the hull bottom particularly critical, as this area

experiences the maximum pressure. Among all measurement points, P11, located at a specific position, records the highest pressure, which is attributed to the water entry depth at this location. Fig.19 presents a time-domain curve analysis of five pressure monitoring points located on the bow, midsection, and stern sections of the seaplane model.

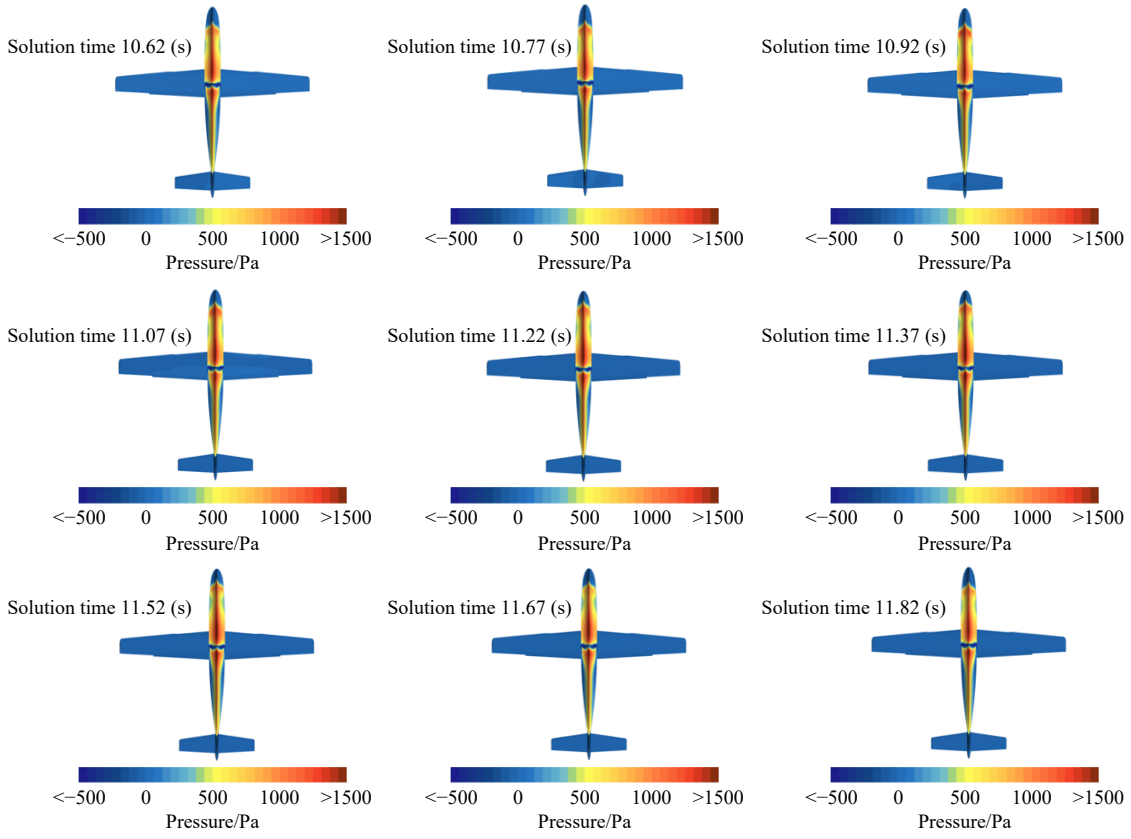



Fig.18 Pressure contour of seaplane bottom

In Fig.20, the time-domain curves at the measurement points (P10, P11, P12, and P19) located in the middle and stern sections of the body exhibit a sine wave pattern. This indicates that the pressure fluctuations at these positions are periodic, with no significant nonlinear phenomena observed. The presence of sine curves typically corresponds to the periodic movement of waves, suggesting that the pressure variations in these areas are primarily driven by the periodic effects of the waves. In contrast, the time-domain curve at the bow measurement P3 clearly shows a nonlinear slamming phenomenon. This suggests that, under these operating conditions, the impact of the water flow at the bow is more complex, making the occurrence of the slamming phenomenon more likely.

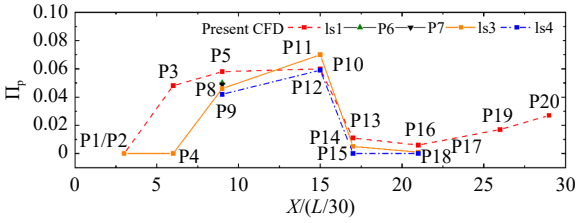
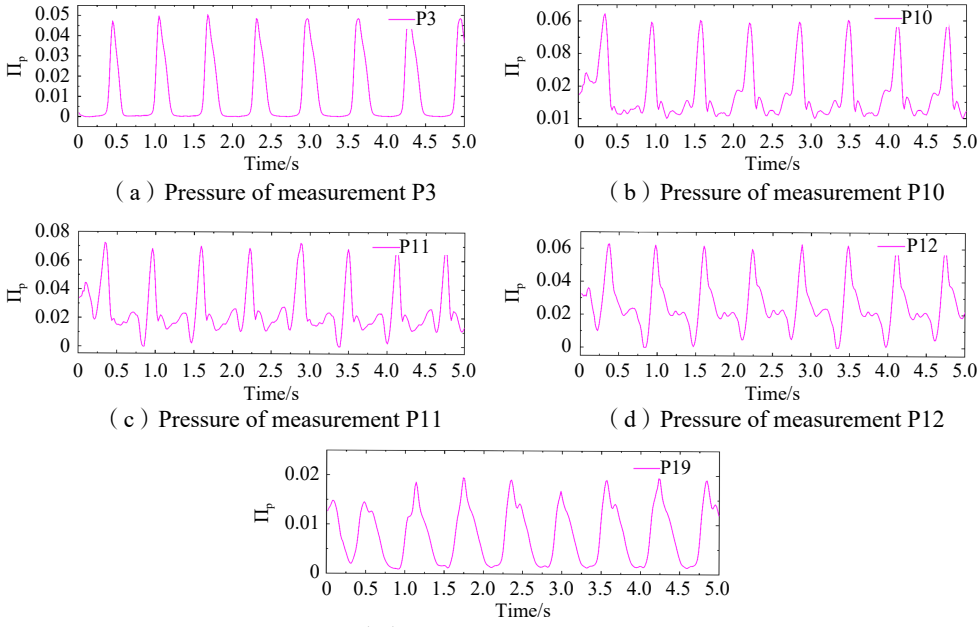



Fig.19 Longitudinal distribution of impact load in Case 2

Fig.21 illustrates the pressure contour on the bottom of the seaplane during one wave cycle in Case 2. Due to the high speed of the seaplane under this condition, pressure during the gliding phase is primarily concentrated at the front and rear of the step breakdown. The step breakdown structure induces local acceleration of the water flow, resulting in changes to the pressure distribution. These changes cause sudden fluctuations in pressure at the monitoring points in this region. Additionally, it is observed that the pressure

on the fuselage surface is symmetrically distributed along the longitudinal centerline of the aircraft.




（a）Pressure of measurement P3　（b）Pressure of measurement P10

（c）Pressure of measurement P11　（d）Pressure of measurement P12

（e）Pressure of measurement P19

Fig.20 Time-domain pressure curve

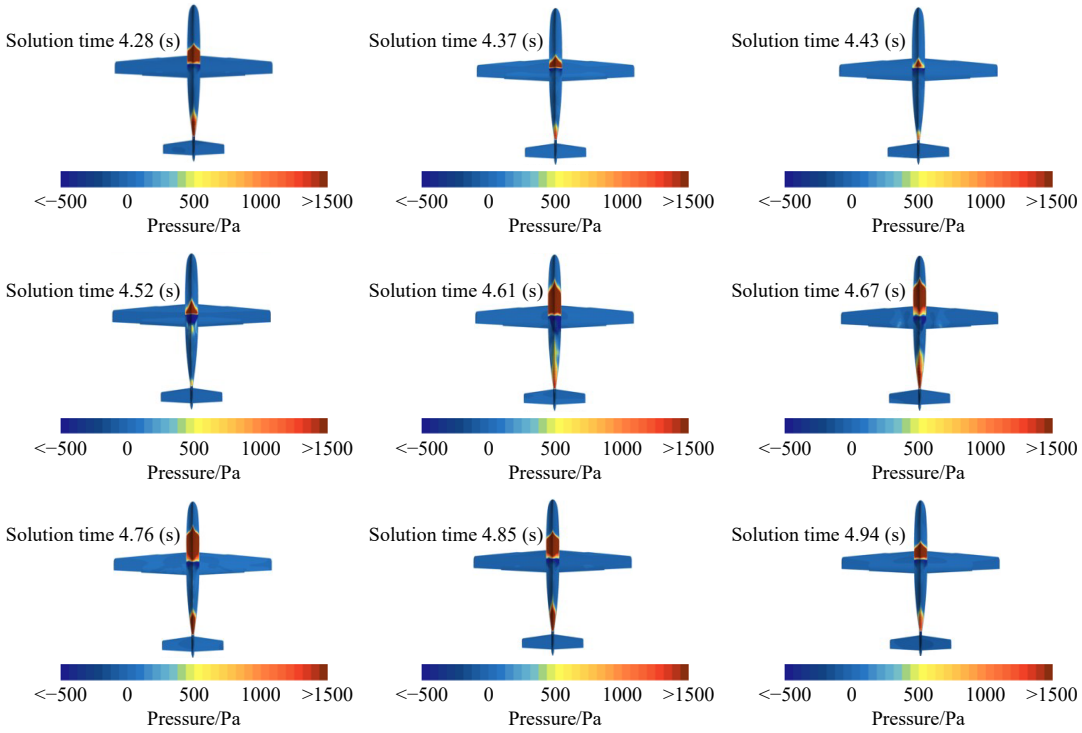



Fig.21 Pressure contour of seaplane bottom

Fig.22 shows the longitudinal distribution of impact load in Case 3. The peak load recorded at the measurement points gradually decreases as the distance from the centerline plane increases along the same transverse section. This trend indicates that the aircraft is primarily influenced by wave loads, making the structural design near the centerline plane of the hull bottom particularly critical, as this area experiences the maximum pressure. Among all measurement points, P9 records the highest pressure, which is attributed to the

water entry depth at this location.

In Fig.23, the time-domain curves at the measurement points (P10, P11, P12, and P19) located in the middle and stern sections of the body exhibit a significant nonlinear phenomenon. There are several peak points in the curves. Under these circumstances, the nonlinear phenomena caused by high speeds become more pronounced. The seaplane encounters larger waves and stronger hydrodynamic effects, resulting in more intense impacts in the middle and stern sections of the aircraft.

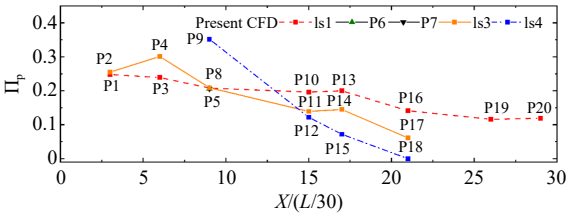
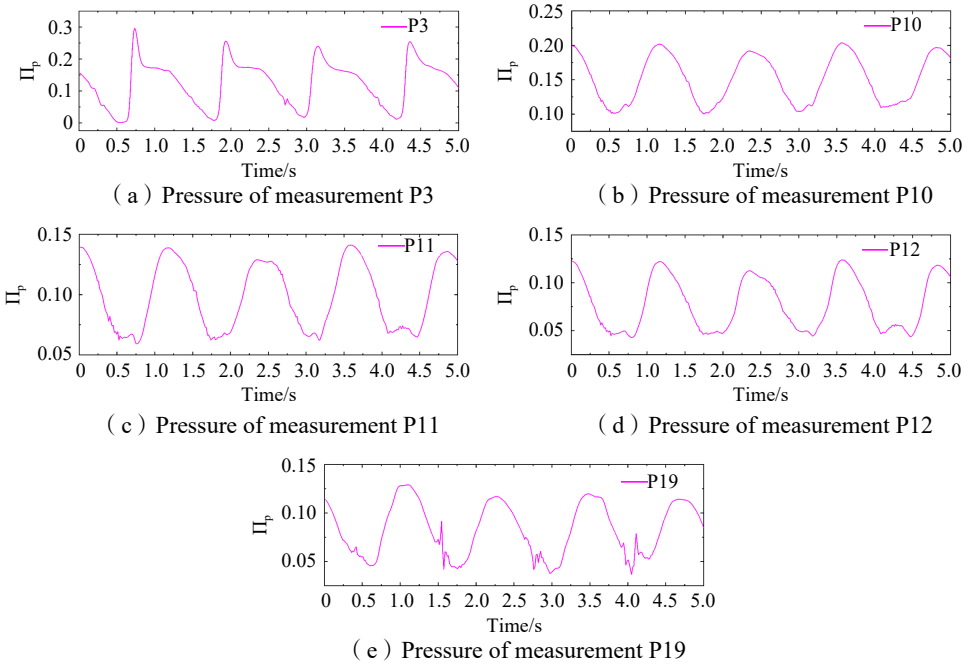



Fig.22 Longitudinal distribution of impact load in Case 3




(a) Pressure of measurement P3
(b) Pressure of measurement P10
(c) Pressure of measurement P11
(d) Pressure of measurement P12
(e) Pressure of measurement P19

Fig.23 Time-domain pressure curve

Fig.24 illustrates the pressure contour on the underside of the seaplane during one wave cycle in Case 3. When the seaplane encounters larger waves and stronger hydrodynamic forces, the impact on the seaplane's underside is significantly greater compared to the other two cases, the impact loads increase with wave height. The relative positions of the seaplane and the waves fluctuate, leading to varying locations where maximum impact pressure is generated. Due to the structural changes occurring at the seaplane's break stage, the impact load at this location differs from that at other points.

### 3.6 Summary of parametric trends

As indicated by the aforementioned investigations, when the seaplane maintains stable motion relative to the waves, the periods of its heave and pitch motions at various speeds closely correspond to the encountered wave period. The heave and pitch responses remain synchronized with the wave profile. The amplitudes of heave, pitch, and the vertical acceleration increase with both wave height and gliding speed. Additionally, the heave and pitch motions increase with wavelength, reaching a maximum at approximately 1.5 times the relative wavelengths, and subsequently decrease. At higher gliding speeds, significant nonlinear phenomena occur at locations near the midsection and stern of the fuselage. The influence of nonlinear impact loads on the seaplane's motion becomes more pronounced at elevated speeds. Under these conditions, the seaplane encounters larger waves and stronger hydrodynamic forces, resulting in more intense impacts in the mid and aft sections of the seaplane.

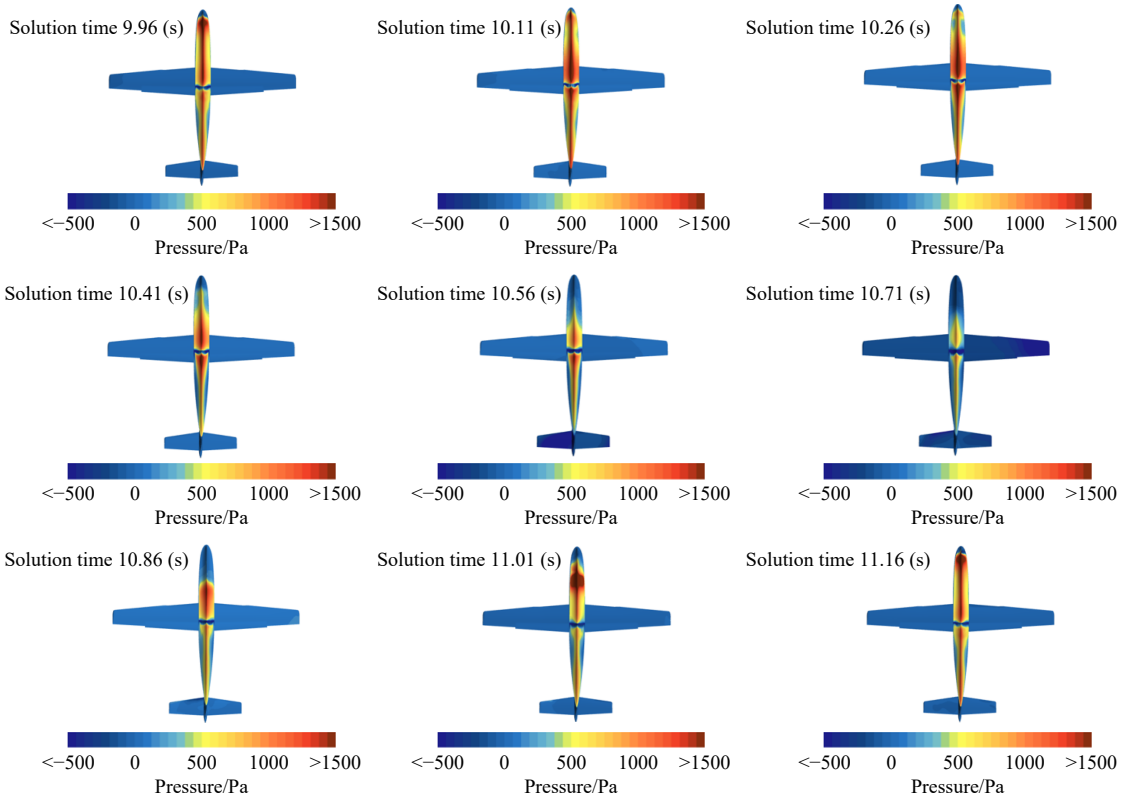



Fig.24 Pressure contour of seaplane bottom

## 4 Conclusions

This paper investigates the motion responses of a seaplane through CFD simulations based on the FVM method and the VOF model. The air-water coupling method is applied in all simulations. The DFBI model is employed to calculate the six-degree motion of the seaplane. The simulation method is validated by comparing it with experimental results, which demonstrate that the method is both accurate and efficient for calculating seaplane gliding in waves. A series of numerical simulations are conducted to study the influence of wave parameters on the motion of the seaplane in addition to model tests. It is found that the hydrodynamic load predominantly affects the motion characteristics of the seaplane during gliding on waves. Four conclusions are drawn as follows:

(1) The air-water two-phase coupling numerical method, based on the CFD solver, can effectively simulate the wave water taxiing problem of a seaplane. When a seaplane glides over waves, it experiences coupled effects, such as wave load, slamming force, and aerodynamic lift, simultaneously, resulting in significant pitch and heave motions. In this study, a CFD simulation method utilizing the FVM and the VOF model, accounting for gas-liquid coupling, is employed to numerically simulate the wave gliding tank model test of the seaplane. The heave and pitch motion curves of the seaplane model, under the combined influence of wave action and aerodynamic lift, are calculated, with an error margin of less than 10% compared to the experimental results, thus confirming the validity of the numerical method.

(2) Under fixed speed and wave height conditions, the heave and pitch motions of the seaplane exhibit a non-monotonic trend as the wavelength changes. Initially, these motions increase with the wavelength, reaching a maximum at approximately 1.5 relative wavelengths, and then decrease. Furthermore, the vertical

acceleration of the center of gravity decreases as the wavelength increases.

(3) As the gliding speed and wave height increase, the motion amplitude of the seaplane also increases. This suggests that slamming occurs at higher gliding speeds and wave heights, with the porpoising motion of the seaplane becoming more pronounced.

(4) Structural changes at the seaplane step break result in peak loads in both the front and rear sections at this location. The structural design near the centerline of the fuselage bottom is critical, as this region experiences maximum pressure. During the structural design phase of the seaplane, particular attention should be given to the structural strength of this area.

Although the motion and hydrodynamic forces of the scaled seaplane model can be accurately predicted under moderate conditions, numerical simulation errors increase significantly at higher gliding speeds, such as 9 m/s. This indicates that more stringent numerical requirements are necessary. As revealed in the above analysis, the VOF model exhibits inherent limitations, particularly in resolving the air-water interface, which demands a higher mesh resolution. The current CFD approach used in this study is insufficient for accurately capturing the free surface and air-water interactions in multiphase flows involving seaplanes. To enable high-fidelity simulations of full-scale seaplanes, further advancements in numerical methodologies are essential.

## Acknowledgements

All authors gratefully acknowledge the fund support of the National Natural Science Foundation of China (Nos. 52071243 and 52101371).

### References

[1] Klemin A, Plerson J D, Storer M S. An introduction to seaplane porpoising[J]. J. Aeronaut. Sci., 1939, 6(8): 311–318.

[2] Lina L J. The effect of dead rise upon the low-angle type of porpoising[R]. Arch. Image Libr. NASA. 610: 1−15, 1942.

[3] Haines G A. Comparison of pitching moments obtained during seaplane landings with values predicted by hydrodynamic impact theory[R]. Washington, D. C., NACA-TN-1881, 1949.

[4] Smith A G, White H G. A review of porpoising instability of seaplanes[R]. ARC Rep. & Memo. 2852, 7741, 1944.

[5] Sottorf W. Systematic model researches on the stability limits of the DV series of float designs[R]. Tech. Rep. Arch. & Image Libr., NACA/TM-1254, 1949.

[6] Ridland D M, Friswell J K, Kurn A G. An investigation of the hydrodynamic stability and spray characteristics of high length/beam ratio seaplane hulls with high beam loadings[R]. ARC Rep. & Memo, 3095. 1956.

[7] Sun H, Faltinsen O M. The influence of gravity on the performance of planing vessels in calm water[J]. J. Eng. Math., 2007, 58: 91–107.

[8] Sun H, Faltinsen O M. Hydrodynamic forces on a planing hull in forced heave or pitch motions in calm water[C]//22nd IWWWFB. Plitvice, Croatia. 2007: 185−188.

[9] Sun H, Faltinsen O M. Numerical study of planing vessels in waves[C]//9th Int. Conf. Hydrodynamics, Shanghai, China. 2010: 468−475.

[10] Qiu L J, Song W B. Efficient decoupled hydrodynamic and aerodynamic analysis of amphibious aircraft water takeoff process[J]. J. Aircraft., 2013, 50(5): 1369–1379.

[11] Zheng X L, Wu B, Wang M Z, et al. Experiment and simulation on calm water taxiing of seaplane based on CFD[J]. J. Phys. Conf. Ser., 2019, 1300: 012041.

[12] Zheng Y L, Qu Q L, Liu P Q, et al. Numerical analysis of the porpoising motion of a blended wing body aircraft during ditching[J]. Aerospace Sci. Technol., 2021, 119: 107131.

[13] Duan X P, Sun W P, Chen C, et al. Numerical investigation of the porpoising motion of a seaplane planing on water with high speeds[J]. Aerospace Sci. Technol., 2019, 84: 980−994.
[14] Zheng X, Quan S N, Wu B, et al. Numerical simulation of seaplane water takeoff process based on CFD[J]. J. Phys. Conf. Ser., 2021, 2030: 012103.
[15] Song Z J, Deng R, Wu T C, et al. Numerical simulation of taxiing motion and hydrodynamic performance of a seaplane in calm water and waves[J]. Eng. Appl. Comput. Fluid Mech., 2023, 17: 2244028.
[16] Deng R, Ren H, Lia H, et al. Numerical study on the hydrodynamic performance of a high-speed taxiing fuselage: Investigation on the affecting factors in the numerical simulation[J]. Ocean. Eng., 2024, 309: 118499.
[17] Simcenter STAR-CCM+, Software Package, Version. User guide manual Siemens digital industries software[K]. Plano, TX, USA, 2020.
[18] Hirt C W, Nichols B D. Volume of fluid (VOF) method for the dynamics of free boundaries[J]. Journal of Computational Physics, 1981, 39(1): 201−225.
[19] Hu Q. Analysis and research report on wave planing load characteristics of seaplane[R]. Jingmen: China Special Vehicle Research Institute, 2023: 28−65.
[20] Jafar M, Dala L, Huard B. A review of the analytical methods used for seaplanes' performance prediction[J]. Aircr, Eng. Aerosp. Technol., 2019, 91 (6): 820−833.
[21] IT'TC. Uncertainty analysis in CFD verification and validation methodology and procedures[R]. 2011.

# 水上飞机波浪水面滑行中的海豚运动特性研究

刘维勤[1,2], 潘振峰[1], 宋学敏[1,2], 胡　奇[3,4], 王明振[3,4], 邹启禄[1]
（1. 高性能船舶技术重点实验室(武汉理工大学)，武汉 430063; 2. 武汉理工大学 航海与能源动力工程学院，武汉 430063; 3. 中国特种飞行器研究所，湖北 荆门 448000; 4. 高速水动力航空科学技术重点实验室，湖北 荆门 448000）

**摘要：**水上飞机在水上作业时会受到包括砰击、溅射和波浪干扰等水动力现象的影响。当在水面滑行时，水上飞机可能会遭遇砰击，即机身以高速撞击水面，进而产生较大的垂直加速度和冲击力。本文首先利用计算流体动力学软件建立模型飞机的水动力模型。为考虑气液两相耦合作用，采用流体体积模型来求解纳维-斯托克斯方程，同时应用动态流体相互作用方法模拟水上飞机的六自由度运动，并在不同的滑行速度下开展数值模拟。随后，比较分析仿真模拟结果与试验数据，验证数值方法在研究水上飞机波浪滑行运动特性方面的有效性。最后，针对不同的波浪条件进行数值模拟，运用 CFD 数值计算方法研究波浪参数对水上飞机运动的影响。研究结果表明，水动力载荷对水上飞机在波浪上滑行时的运动特性具有显著的影响。

**关键词：**水上飞机；体积分数法(VOF)；海豚运动；滑行；水动力载荷
**中图分类号：**U661.1　　**文献标识码：**A
**基金项目：**国家自然科学基金资助项目(52101371; 52071243)

**作者简介：**刘维勤(1985−)，男，博士，副教授；
潘振峰(2001−)，男，硕士；
宋学敏(1986−)，女，博士，副教授，通讯作者，E-mail: sxmxs@whut.edu.cn；
胡　奇 (1987−)男，硕士；
王明振(1984−)男，硕士；
邹启禄 (1998−)女，硕士。